Expanding the Capabilities of Automotive Radar for Bicycle Detection With Harmonic RFID Tags at 79/158 GHz

Tobias T. Braun, *Graduate Student Member, IEEE*, Jan Schöpfel, *Graduate Student Member, IEEE*, Patrick Kwiatkowski, *Graduate Student Member, IEEE*, Christian Schweer, Klaus Aufinger, *Member, IEEE*, and Nils Pohl, *Senior Member, IEEE*

***Abstract*— Although traffic safety continues to improve overall, fatalities of vulnerable traffic participants and pedal cyclists specifically have reached 30-year highs. While automotive radar sensors continue to advance and are integrated in more and more vehicles, they are not ideally suited to detect pedal cyclists, especially in complicated traffic scenarios. To mitigate the problem of the lower radar-cross section (RCS) of the cyclist, equipping them with harmonic radio frequency identification (RFID) tags is proposed. The presented system showcases the benefits of this approach by being able to conduct conventional automotive radar measurements and detect tags simultaneously. In this work, we present the printed-circuit boards (PCBs) and the necessary chipset, while especially focusing on the design of a power-efficient harmonic RFID tag. By improving the gain per current of an amplifier chain, the tag enables a range sufficient for urban scenarios while consuming little enough current to be powered by battery-operated lights. This enables the detection of pedal cyclists even in complicated scenarios at a distance of up to 80 m.**

***Index Terms*— Automotive, clutter suppression, *D*-band, frequency doubler, frequency-modulated continuous wave (FMCW), harmonic, millimeter-wave (mm-wave), monolithic microwave integrated circuit (MMIC), radar, radio frequency identification (RFID), SiGe, tag, vulnerable road users, *W*-band.**

I. Introduction

NEARLY a decade has passed since Mercedes drove the Bertha Benz memorial route to prove the feasibility of autonomous driving [1]. To do so, an S-Class "learned to see," via the help of cameras [2], as well as short-range radar (SRR) and long-range radar (LRR) sensors [3]. The experimental vehicle's sensor layout has since acted as a role model, with similar layouts used in production cars today.

The increased focus on autonomous driving in urban environments has changed the requirements of the used radar systems. Compared with the LRR used for automatic cruise control, the task of SRR has shifted from detection to imaging [4]. Multiple-input–multiple-output (MIMO) radar sensors have since addressed that challenge [5]. Simultaneously, the advancements in SiGe [6] and CMOS technologies [7] have reduced the cost of 77 GHz sensors. These developments have allowed the integration of radar sensors designed for urban scenarios, even in middle-class vehicles [8].

The main aim of the higher level of driving automation is to increase traffic safety. Accordingly, the fatalities per 1 million vehicle miles traveled in USA have decreased continuously. However, inside those numbers, an additional trend has manifested itself. According to the National Highway Traffic Safety Administration (NHTSA), the group of outside vehicles consisting of motor and pedal cyclists, pedestrians, and other nonoccupants does not benefit equally from these developments. Since 1996, the proportion of fatalities assigned to outside vehicles has increased by 70%. The reason for the relative increase is not a slower safety improvement compared with inside vehicles but a deterioration. In absolute numbers, the most current data show at least a 30-year high for all outside vehicle subcategories. In particular, the number of fatal bicycle accidents in 2020 was the highest since 1987.

Somehow, these numbers do not reflect the improvement in radar sensors. While one could hope for a future improvement based on an even higher integration in production cars and further developments of the sensor, in principle, the disadvantage of outside vehicles can also be found in the radar equation itself

$$P_{\mathrm{RX}} = \frac{P_{\mathrm{TX}} \cdot G_{\mathrm{TX}} \cdot G_{\mathrm{RX}} \cdot \lambda^2 \cdot \sigma}{(4\pi)^3 \cdot R^4}. \tag{1}$$

While all these equation's variables contribute to the received power, when trying to detect one target surrounded by clutter, the target's radar-cross section (RCS) σ is the one key metric. Matching the fatality numbers, the vulnerable outside vehicles form a cohesive group with a lower RCS

Manuscript received 19 July 2022; revised 3 October 2022; accepted 16 October 2022. Date of publication 23 November 2022; date of current version 13 January 2023. This work was supported by the German Federal Ministry of Education and Research (BMBF) within the Project SeeYou. This article is an expanded version from the 2022 IEEE/MTT-S International Microwave Symposium (IMS), Denver, CO, USA, June 19–24, 2022 [DOI: 10.1109/IMS37962.2022.9865601]. *(Corresponding author: Tobias T. Braun.)*

Tobias T. Braun, Jan Schöpfel, Patrick Kwiatkowski, and Nils Pohl are with the Institute of Integrated Systems, Ruhr University Bochum, 44801 Bochum, Germany (e-mail: tobias.t.braun@rub.de).

Christian Schweer is with Kostal Automobil Elektrik GmbH & Company KG, 44227 Dortmund, Germany.

Klaus Aufinger is with Infineon Technologies AG, 85579 Neubiberg, Germany.

Color versions of one or more figures in this article are available at https://doi.org/10.1109/TMTT.2022.3219541.

Digital Object Identifier 10.1109/TMTT.2022.3219541

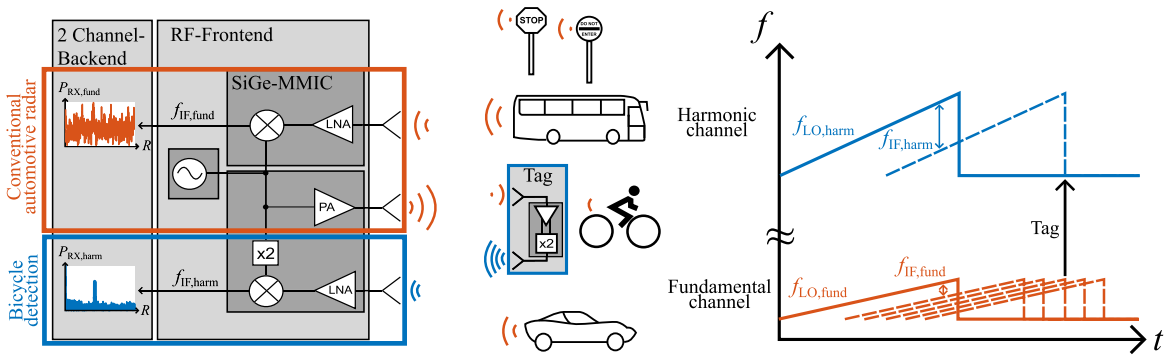

Fig. 1. Concept of the realized system. An MIMO capable automotive chipset is expanded via a harmonic transceiver, to add the ability of bicycle detection. The bicycles are equipped with harmonic RFID tags. Since the tag exclusively doubles the received chirp, it can be easily detected in the added receive (RX) channel, even in the presence of objects with a larger RCS.

than inside vehicles. Specifically, the rear RCS of a bicycle, including a dummy cyclist, is up to 20 dB lower than that of a mid-sized car in measurements with a 77-GHz radar sensor [9]. Unfortunately, the lack of a surrounding metal frame makes them more vulnerable and less visible to a radar system simultaneously.

To deal with this problem, some attempts to increase the RCS of a bicycle or pedestrian via additive structures were made [10], [11]. Apart from that, the most recent developments regarding cyclists and pedestrians focus on micro-Doppler extraction for target classification [12], [13], [14]. However, all these approaches necessitate the pedal cyclist to be detectable in the first place. Furthermore, even for close-to-ideal laboratory settings, the micro-Doppler dynamic range caused by the spokes is typically 15 dB or less, while also being strongly dependent on the observation angle [13]. In complicated traffic scenarios, these approaches will be even more challenging. Further difficulties such as weather influences, typically a strength of radar systems compared with other sensors, are also the topic of current research [15].

Instead, this work proposes to equip pedal cyclists with a harmonic radio frequency identification (RFID) tag. This approach has been implemented successfully in other areas, where tracking a specific target surrounded by other objects is desired. Examples include respiratory monitoring using passive RF-tags [16] or harmonic radar systems for insect tracking [17], [18].

To use this approach for bicycle detection, we designed a harmonic radar system based on harmonic RFID tags. We recently published a brief overview of the necessary hardware with measurements inside a hallway to showcase the benefits of this approach in [19]. This article is an extended version going into more detail on all the necessary monolithic microwave integrated circuits (MMICs) and the printed-circuit boards (PCBs), including waveguide transitions covering the W- and D-bands, respectively. Specifically, the successful implementation of a high range tag at a low current consumption is supported by theory and simulations and characterized by on-chip measurements. In addition, we present system measurements in the field, by attaching the system to a car, highlighting the benefits of its bicycle detection capabilities.

The subsequent article is thereby organized in the following way: Section II describes the principles of a harmonic frequency-modulated continuous wave (FMCW) radar and draws conclusions on important parameters during the design process. In Section III, the chipset is presented. Section IV covers the realized PCBs. The measurement results showing the improved clutter rejection and bicycle detection are shown in Section V, and finally, conclusions are drawn in Section VI.

II. Harmonic FMCW Radar Principle

In contrast to other applications, the targets not equipped with a tag must not just be considered clutter. An automotive radar has to detect all the obstacles, not just pedal cyclists. Therefore, the system we designed expands a conventional automotive radar to add the ability of bicycle detection. To do so, it has an additional RX channel at the harmonic frequencies. The concept of the system is presented in Fig. 1.

The system sends out an ascending frequency ramp in the automotive band, which can be expressed as

$$s_{\mathrm{LO,fund}}(t) = A_{\mathrm{TX}} \cdot \cos\left(\omega_0 t + \frac{1}{2}\frac{B}{T}t^2\right), \quad -\frac{T}{2} \le t \le \frac{T}{2}. \tag{2}$$

It has an amplitude A_{TX} at the output of the transmit (TX) antenna, around the center angular frequency ω_0. The ramp slope (B/T) is determined by the bandwidth of the frequency chirp B and its duration T. This signal is reflected by every traffic participant and road sign. Subsequently, the reflected frequency ramps at the fundamental receiver

$$s_{\mathrm{RX,fund}}(t) = A_{\mathrm{RX}} \cdot \cos\left(\omega_0(t-\tau) + \frac{1}{2}\frac{B}{T}(t-\tau)^2\right) \tag{3}$$

exhibit a propagation delay $\tau = (2 \cdot R/c)$. The superposition of those signals is downconverted at the receiver's mixer. For K targets, the resulting IF signal is given by

$$s_{\mathrm{IF,fund}}(t) = \sum_{k=0}^{K-1} A_k \cdot \cos\left(\frac{B}{T}\tau_k t + \omega_0 \tau_k - \frac{1}{2}\frac{B}{T}\tau_k^2\right) \tag{4}$$

all in accordance to [20]. During signal processing, the ranges of the targets can therefore be calculated based on their IF

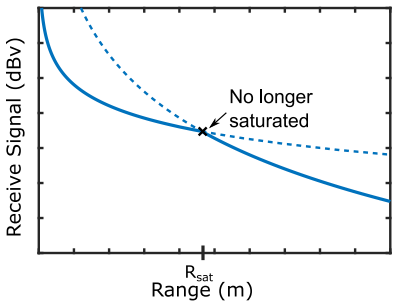

Fig. 2. Proportionalities of the tag depending on the range. The longer the amplifier chain saturates the tag, it stays in the beneficial $(1/R^2)$ proportionality.

frequencies as

$$R = \frac{f_{\mathrm{IF,fund}} \cdot Tc}{2B}. \tag{5}$$

The amplitudes of these frequencies A_k, however, differ by the ratio (σ/R^4) in accordance to (1). This is where the lower RCS of the cyclist is disadvantageous. When equipping the cyclist with the harmonic tag, its signal at the harmonic receiver

$$s_{\mathrm{RX,tag}}(t) = A_{\mathrm{RX,tag}} \cdot \cos\left(2\omega_0(t-\tau) + \frac{B}{T}(t-\tau)\right) \tag{6}$$

has twice the bandwidth at a doubled center frequency compared with (2). The additional harmonic receiver downconverts the tag's signal with the harmonic LO signal given by $f_{\mathrm{LO,harm}} = 2 \cdot f_{\mathrm{LO,fund}}$. Since no other received signal lies within the baseband after downconversion with $f_{\mathrm{LO,harm}}$, the IF signal only consists of the tag's contribution for the scenario in Fig. 1

$$s_{\mathrm{IF,harm}}(t) = A \cdot \cos\left(\frac{2B}{T}\tau_k t + 2\omega_0\tau_k - \frac{B}{T}\tau_k^2\right). \tag{7}$$

Therefore, the range of the bicycle can by calculated as

$$R = \frac{f_{\mathrm{IF,harm}} \cdot Tc}{4B} \tag{8}$$

based on the harmonic measurement.

In summary, thanks to the harmonic tag, the bicycle can be detected independently of the surrounding vehicles and clutter. In addition, as long as the doubled ramp slope and center frequency are taken into account, conventional FMCW signal processing can be applied.

However, the relationship of the received power in dependence of the range given in (1) changes, as previous research on the harmonic FMCW radar with active tags has shown [21]. This is caused by the saturated output power P_{sat} and nonlinearity of the frequency doubler. As long as the power received at the tag is strong enough for the frequency doubler to saturate, the tag's output power is independent of the range. Subsequently, the tag's signal only has to travel one-way back to the radar system. However, for further distances the nonlinearity of the doubler additionally increases the range dependency of (1). In total, this results in the following proportionality:

$$P_{\mathrm{RX,harm}} \begin{cases} \propto \dfrac{1}{R^2}, & R \le R_{\mathrm{sat}} \\ \propto \dfrac{1}{R^6}, & R > R_{\mathrm{sat}} \end{cases} \tag{9}$$

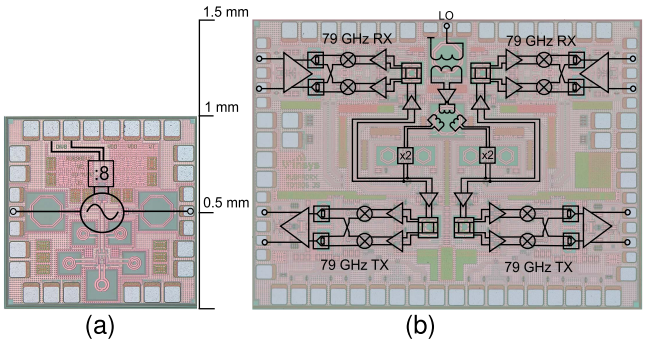

Fig. 3. Chipset enabling conventional automotive radar measurements. It consists of (a) VCO generating the LO signal and (b) MIMO-capable fundamental transceiver with two TX and two RX channels, respectively.

which is also illustrated in Fig. 2. In comparison to linear targets with a constant RCS σ, as described in (1), this corresponds to a dependency of the RCS on the range. To increase the maximum detectable range of the tag, the aim is to stay in the first region for as long as possible. As long as the received power is high enough to saturate the tag, the RCS increases with range, while it decreases as soon as that is no longer the case. It is therefore desirable to increase the maximum range at which the tag sends out its P_{sat}. This is done by an amplifier chain in front of the frequency doubler. Its design considerations are discussed in detail in Section III-D.

III. Millimeter-Wave (mm-Wave) Integrated Circuits (MMICs)

The presented system consists of four MMICs which are presented in further detail in this chapter. They are divided into two groups. First, the VCO and the fundamental transceiver allow for conventional automotive radar measurements. Second, the harmonic transceiver and the harmonic RFID tag expand this system to include the ability of bicycle detection.

The architecture is based on one VCO generating the LO signal and thus the frequency ramps shared by all the transceiver MMICs. This concept is MIMO-scalable and is presented in [22]. All the MMICs are manufactured in Infineon's 130-nm B11HFC SiGe:C technology with an $f_{\mathrm{T}} = 250$ GHz and $f_{\mathrm{max}} = 370$ GHz.

A. VCO

The VCO itself is also based on the design presented in [22]. Its tunable bandwidth is subharmonic to the automotive band and extends from 34 to 41 GHz. This allows for an easier distribution of the LO signal on the PCB of the presented system. To further enable easier LO distribution for large MIMO arrays, the VCO has two outputs, each featuring a balun. The single-ended LO signal can be split on the PCB with a Wilkinson divider. With an output power of 3 dBm at each of the outputs, the VCO can drive up to 32 transceiver MMICs, which feature two channels each, thus enabling large MIMO arrays.

In addition, a static divide-by-8 divider is also integrated on the VCO, which enables stabilization with commercially available PLLs. Fig. 3(a) depicts the VCO-MMIC.

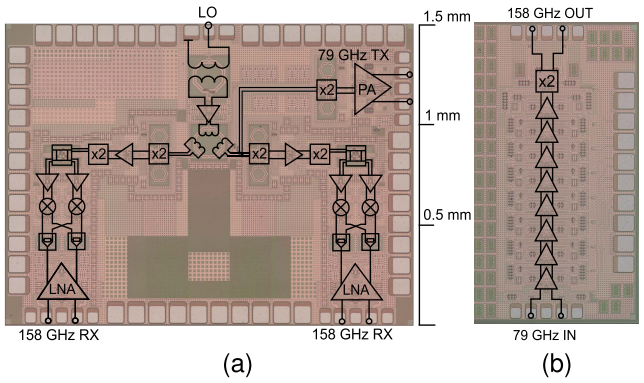

Fig. 4. Chipset enabling bicycle detection. It consists of (a) MIMO-capable harmonic transceiver with one fundamental TX and two harmonic RX channels and (b) harmonic frequency tag.

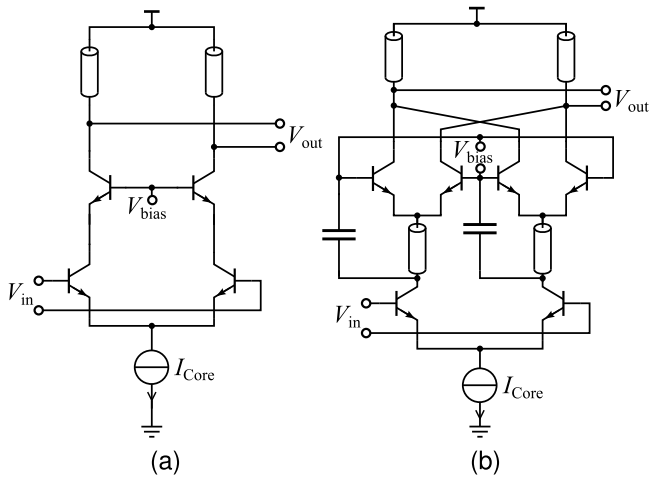

Fig. 5. Schematics of (a) cascode amplifier making up the amplifier chain and (b) bootstrapped Gilbert doubler.

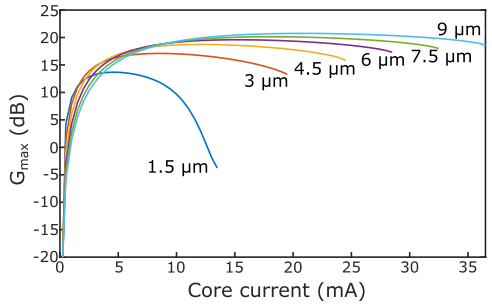

Fig. 6. Simulated G_{max} of a cascode amplifier for various transistor sizes. Larger transistors enable a decreasingly larger gain. However, per core current, the smallest transistor offers the highest G_{max}.

B. Fundamental Transceiver MMIC

The fundamental transceiver is an improved version of the transceiver presented in [22]. Two TX and two RX channels at the fundamental frequency are realized on one MMIC, as illustrated in Fig. 3(b). Two of these four channels can be used simultaneously in an arbitrary configuration. This configuration is determined by cutting fuses on the chip depending on the desired application. The used RX channel consists of a low-noise amplifier (LNA) and a downconversion IQ mixer using a fully differential Lange coupler [23]. It can therefore be used to receive arbitrary waveforms. However, in this FMCW system only the differential I output of one of the RX channels is used. The LNA has a simulated noise figure of 5.3 dB. The conversion gain of the complete RX path is simulated to be 23.5 dB with a noise figure of 6 dB.

C. Harmonic Transceiver MMIC

To detect the bicycles equipped with the harmonic frequency tag, we designed the harmonic transceiver MMIC presented in Fig. 4(a). It has two of the necessary RX channels at the harmonic frequency. They each include a frequency quadrupler, two-stage LNA, and differential IQ mixer, respectively. Using separate frequency quadruplers for each channel, the isolation between them is increased. The LNA achieves a maximum simulated gain of 14 dB with a minimum simulated noise figure of 10 dB in the region of interest. In addition, the simulations show reverse isolation higher than 65 dB throughout the region of interest. The IQ mixer achieves a simulated conversion gain of 5.1 dB with a noise figure of 15.1 dB. Altogether one RX channel achieves a conversion gain of 19 dB with a noise figure of 11.35 dB. Given that this was not the main focus of the work, this compares decently to the state-of-the-art [24]. Again, the presented FMCW system only uses the I output of one RX, while the IQ implementation allows for other waveforms in the future. One RX channel consumes a current of 140 mA from a 3.3-V power supply.

The TX channel consists of a bootstrapped Gilbert frequency doubler to reach the automotive band with the sub-harmonic LO signal, as well as a power amplifier. The Class A cascode amplifier generates an output power of 15 dBm when measured on-chip. In addition, it achieves a measured gain of 15 dB with a power-added efficiency (PAE) of 12.5%. The current consumption for the transceiver channel adds up to 86 mA from a power supply of 3.3 V.

D. RFID Tag MMIC

The main goal in the design of the RFID tag MMIC was to enable sufficient range R from the tag to the radar system for city traffic. As was discussed in Section II, the frequency doubler should send out its P_{sat} for as high of a range as possible. To do so, an amplifier chain is located in front of the frequency doubler. However, another goal of the design was for the current consumption to be low enough for integration into battery-operated bicycle taillights. Subsequently, the amplifier chain should have as high of a gain as possible while consuming as little current as necessary to achieve that gain. We therefore defined the gain per current G_{PerCur} of the individual casocde amplifier as the key metric to optimize in this design. Its schematic is depicted in Fig. 5(a).

As a first step, G_{max} simulations for various transistor sizes were carried out. Fig. 6 depicts the results of those simulations.

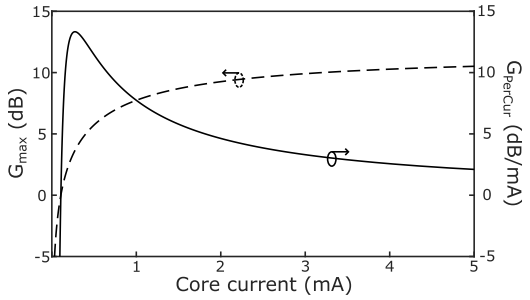

Fig. 7. Calculated $G_{\max}$ and G_{PerCur} of an emitter circuit based on the given equations. The maximum G_{PerCur} is achieved for only 13% the current density for peak f_{T}.

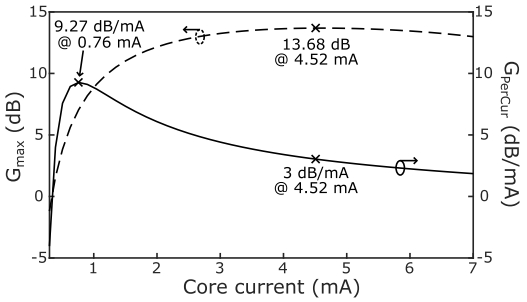

Fig. 8. Simulated $G_{\max}$ and G_{PerCur} of the realized casode amplifier with an emitter length of 1.5 μm. A core current of 17% of the maximum gain and f_T achieves over three times G_{PerCur}.

They show longer emitter lengths achieve a decreasingly higher gain. Specifically, the smallest examined transistor size only achieves 13.68 dB of $G_{\max}$ compared with 17 dB for double the emitter length at twice the current. However, cascading two amplifiers with the 1.5 μm emitter length therefore, in theory, achieves 10 dB more $G_{\max}$ for the same current. Consequently, to optimize G_{PerCur}, we used transistors with an emitter length of 1.5 μm in this design.

Traditionally, in RF circuit design, amplifiers are biased based on the current density to achieve the transistor's peak f_{T}, peak $f_{\max}$, or minimum noise figure $NF_{\min}$ [25]. However, optimizing for G_{PerCur} is not a traditional goal. Therefore, the optimum current density was investigated. To do so systematically, we can first analyze $G_{\max}$ of an emitter circuit analytically. The unity gain frequency $f_{\max}$ of the transistor is known from the literature as [26]

$$f_{\max} = \sqrt{\frac{f_{\mathrm{T}}}{8\pi \cdot R_{\mathrm{B}} \cdot C_{\mathrm{BC}}}}. \tag{10}$$

Since $f_{\max}$ is determined for the point at which

$$G_{\max} = \left(\frac{f_{\max}}{f}\right)^2 = 1. \tag{11}$$

$G_{\max}$ can be calculated as

$$G_{\max} = \frac{f_{\mathrm{T}}}{8\pi \cdot R_{\mathrm{B}} \cdot C_{\mathrm{BC}} \cdot f^2}. \tag{12}$$

In addition to the base resistance R_B and the collector base capacitance C_{BC} of the transistor, it also depends on the transit frequency f_T at a given frequency f. This transit frequency is largely responsible for the current dependency of the gain, with its equation being known as

$$f_{\mathrm{T}} = \frac{1}{2\pi \cdot \left(\frac{n \cdot V_{\mathrm{T}} \cdot (C_{\mathrm{BE}} + C_{\mathrm{BC}})}{I_{\mathrm{C}}} + \tau_{\mathrm{F}} + C_{\mathrm{BC}} \cdot (R_{\mathrm{E}} + R_{\mathrm{C}})\right)} \tag{13}$$

from the parameter extraction of HBTs [27], [28]. It depends on additional transistor parameters, namely, the transit time τ_{F}, the ideality factor n, the thermal voltage V_{T}, the base and emitter resistances R_{B} and R_{E}, respectively, and the base-emitter capacitance C_{BE}. Subsequently, the gain per current metric G_{PerCur} can now be calculated as

$$G_{\mathrm{PerCur}} = \frac{10 \cdot \log(G_{\max})}{I_{\mathrm{C}}}. \tag{14}$$

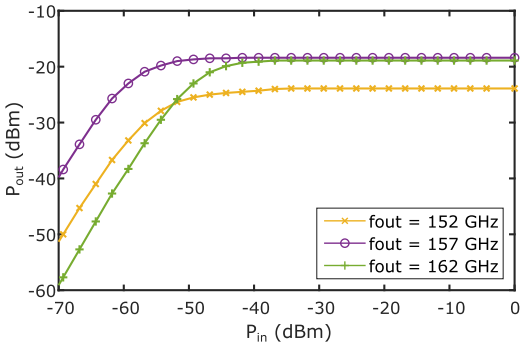

Fig. 9. Compression curve of the harmonic tag measured on-chip. Thanks to the high gain of the amplifier stage, the tag sends out its P_{sat} −3 dB for an input power higher than −57 dBm at the center frequency.

To do so, the transistor's capacitances, resistances, and τ_{F} for (12)–(14) were extracted from an operating-point simulation. The subsequent results of (12) and (14) in dependence of I_{C} are presented in Fig. 7. They show a maximum G_{PerCur} for a current of only 13% of the current for peak f_{T}. In this specific application, it is therefore beneficial to sacrifice the gain of an individual stage, use more stages, and therefore increase G_{PerCur} of the amplifier chain.

To verify those analytical observations, simulations of the used differential cascode amplifier design were carried out. The results of those simulations are presented in Fig. 8. The current density required to achieve the maximum gain of 13.68 dB is very close to the data sheet of the technology. However, when dividing the simulated $G_{\max}$ by the core current, this current density is far from optimal. In similarity to the analytical results, more than three times the G_{PerCur} can be achieved at about 17% of the current density for peak f_{T}.

In the final design, the bias currents and losses of the matching networks between the amplifiers have to be accounted for. Their inclusions decrease the G_{PerCur} maximum and simultaneously shift it toward higher currents. Nevertheless, the performance was improved, using a current density of about 42% of peak f_{T} in each amplifier. To achieve the necessary gain, the chain in front of the frequency doubler uses eight of those amplifiers.

The frequency doubler is used as a bootstrapped Gilbert cell, with its schematic depicted in Fig. 5(b). It was also designed for a low current consumption, while its core current specifies

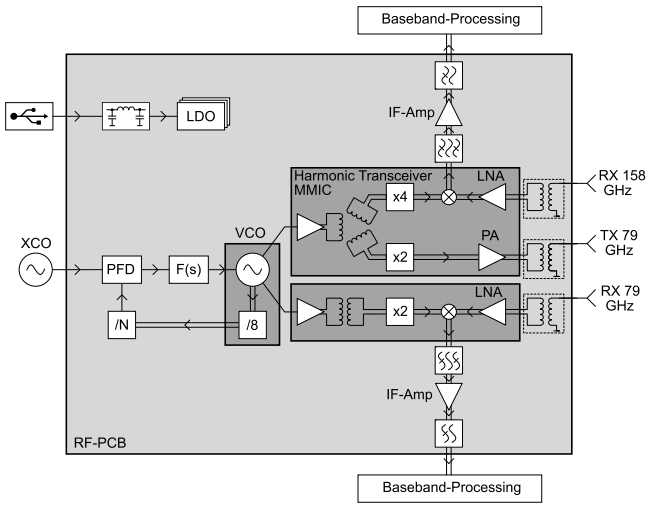

Fig. 10. Block diagram of the realized harmonic radar system. To combine the capabilities of conventional radar measurements with bicycle detection, it has one TX at the automotive band with one RX at the fundamental and harmonic frequency bands, respectively.

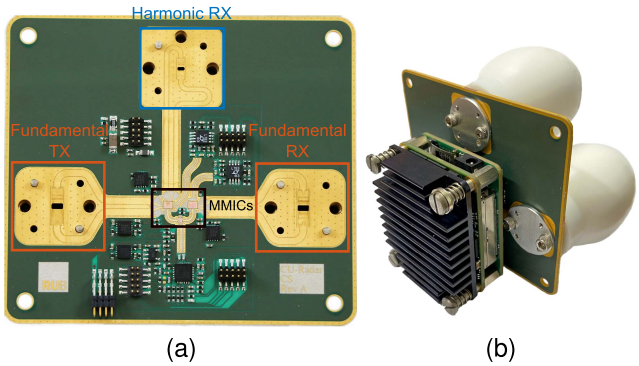

Fig. 11. Photographs of (a) assembled front-end PCB with the MMICs from Section III and the waveguide transitions and (b) complete harmonic radar system with the two-channel backend and FPGA module attached.

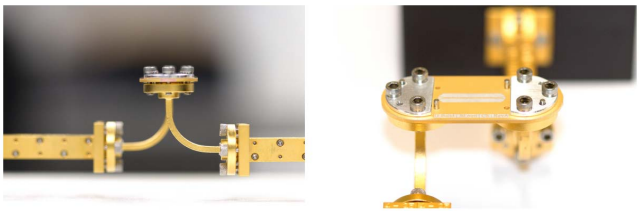

Fig. 12. One of the manufactured back-to-back structures connected to Keysight's PNA-X with the necessary extenders.

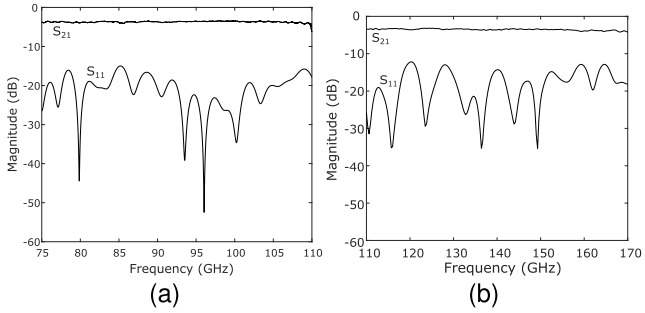

Fig. 13. Results of the AFR for the measured back-to-back transitions for (a) *W*- and (b) *D*-bands.

the tag's P_{sat}. Since the tag's signal only has to travel one-way back to the radar signal as long as the tag saturates, it does not have to be that high. Because of the $(1/R^2)$ proportionality explained in Section II, the power received by the radar system becomes less dependent of the range the further the tag moves away. Therefore, P_{sat} can be chosen to achieve the desired signal-to-noise ratio (SNR) in the radar measurement.

To conclude this chapter, Fig. 9 depicts the compression curve of the realized tag shown in Fig. 4(b), when measured on-chip. Because of the missing bond-wires the tag's matching accounts for, the symmetry at the input and output is shifted, respectively. Nevertheless, for the center output frequency of 157 GHz, it sends out 3 dB below its P_{sat} of -18 dBm for an input power higher than -57 dBm, while consuming 27 mA from a 3.3-V power supply.

IV. Harmonic Radar System and Tag PCB

A. Harmonic Radar System

As we alluded to in Section II, the targets at the fundamental frequency must not just be considered clutter. Therefore in addition to the fundamental TX, the designed system has RX channels for a conventional radar measurement and bicycle detection with the harmonic tag, respectively. This is illustrated in the system's block diagram in Fig. 10.

Therefore, one of each of the transceiver MMICs presented in Section III is used. To cope with the frequencies of their respective RF input or output, the PCB was manufactured out of the Rogers RO3003 substrate, which is standard for automotive applications. It has a thickness of 127 μm, a dielectric constant of $\epsilon_r = 3$, and a dissipation factor $\tan\delta = 0.001$ at 10 GHz. To preserve flexibility regarding the used antennas, the presented system uses waveguide transitions to decouple the RF signals.

These transitions are designed to cover the full *W*- and *D*-bands, respectively. Their concept is based on the transition presented in [29], using a Rogers RT/duroid 5880. The differential RF signal is wire-bonded to a differential microstrip line on the PCB. To decrease losses, this transitions to single-ended microstrip lines and subsequently substrate integrated waveguides (SIWs) as soon as possible. In the harmonic radar system, the SIW also acts as a high pass to decrease coupling between the fundamental TX and harmonic RX. Finally, a symmetrically stepped air-filled waveguide combines their respective electric fields in-phase, similar to a magic-T [30]. The transitions can be seen as part of the assembled front-end PCB in Fig. 11(a).

One key aspect to minimize the insertion loss is the transition from the substrate-filled SIW to the stepped air-filled waveguide. To obtain close to frequency-independent matching, the height of the first step is chosen to be identical to the substrate height of the PCB. Subsequently, the SIW's width a_{SIW} can be calculated from the width of the respective

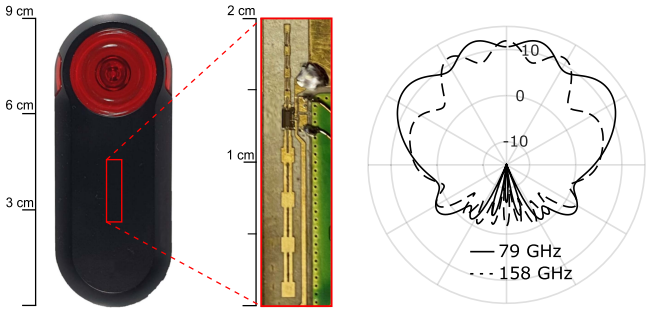

Fig. 14. Tag PCB with the differential patch arrays and their simulated antenna pattern in azimuth. It is small enough to easily fit into a bicycle's taillight.

waveguide a_{WG} via [31]

$$a_{\mathrm{SIW}} = a_{\mathrm{WG}} \cdot \sqrt{\frac{\epsilon_{r,\mathrm{air}}}{\epsilon_{r,\mathrm{PCB}}}}. \tag{15}$$

There, however, remains an inductive susceptance caused by the smaller width of the air-filled waveguide that needs to be matched out. In [29], this is done by the capacitance of the large steps of the following transition. However, this limits the maximum number of steps and therefore the theoretically achievable insertion loss. Because this became problematic in our RO3003-based design, an additional substrate taper was introduced, similar to [32]. The following steps in the bottom copper are designed based on a Chebychev transformer. Further optimization is done with CST Studio Suite.

To characterize the designed waveguide transitions, back-to-back structures were fabricated along with the front-end PCBs. The measurements were conducted using a PNA-X N5247B from Keysight with their N5295AX03 and Virginia Diode's WR6.5-VNAX extenders, respectively. Each setup was calibrated using a TLR calibration kit of the extender's manufacturer. Fig. 12 shows an exemplary back-to-back structure, connected with 90° E-plane bends that were part of the calibration.

The results of the conducted back-to-back measurements were calculated into single-ended results with the PNA-X's automatic fixture removal (AFR). The results of the AFR can be seen in Fig. 13.

To complete the radar system, a two-channel backend with an FPGA module is plugged onto the front-end. The complete system can be seen in Fig. 11(b). The FPGA module can be controlled via USB and controls the PLL chip, as well as the variable gain amplifier. After analog-to-digital conversion, the data of both the RX channels are transferred to a PC via the USB interface. In the measurements of Section V, the dielectric lens antennas also shown in Fig. 11(b) are used. They offer a gain of approximately 28 dBi at the fundamental frequencies [33], [34].

B. Tag PCB

The tag PCB is also realized on Rogers RO3003 substrate with a thickness of 127 μm and is shown in Fig. 14 with a bicycle taillight as a size reference. It only consists of an LDO for the supply voltage and the TX and RX antennas. The antennas and the cavity for the chip are lasered into the PCB. They are realized as differential series-fed patches. Therefore, they offer an antenna pattern typical for automotive applications with a broad radiation in azimuth and a focus in elevation. They offer a maximum gain of 12 dBi each. Their respective simulated radiation pattern is depicted in Fig. 14, together with a picture of the PCB, small enough to easily fit into a bicycle's taillight.

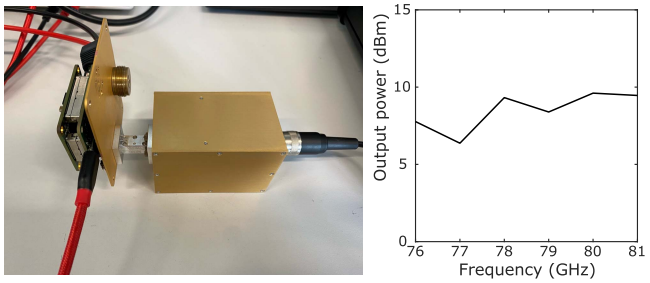

Fig. 15. Measurement setup and results of output power measurements of the radar systems for all integer frequencies of the automotive band.

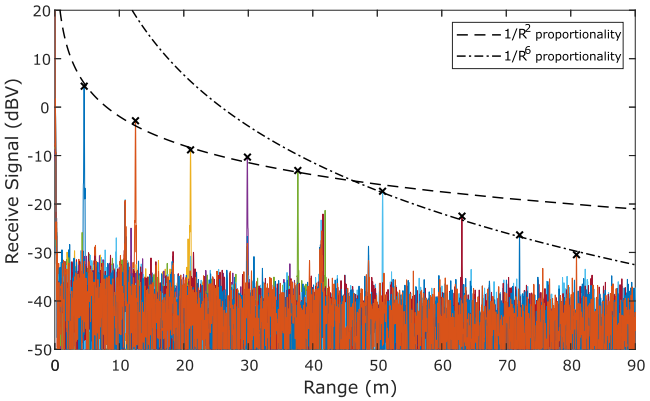

Fig. 16. Measurements to determine the maximum range from [19]. The received power follows the theoretical proportionalities presented in Fig. 2. The tag saturates up to a distance of 47 m with its signal disappearing into the noise floor at just over 80 m.

V. System Measurements

First, the output power of the system at the rectangular waveguide was measured. Therefore, an Erickson PM5 powermeter was connected to the TX and the system was programmed to generate CW frequencies covering the automotive band. The measurement setup and the results are shown in Fig. 15. The system reaches a maximum output power of 9.6 dBm at 80 GHz. This is in good agreement with the PA's output power after the bond-wires and the loss of the waveguide transition, with the SIW being as short as the antenna size of the dielectric lenses allows for.

In [19], the maximum range of the complete system was investigated. For the sake of completeness, the results of those measurements are repeated in Fig. 16. The measurements fit the proportionalities explained in Section II very well. It can be seen that the tag sends out its P_{sat} up to a distance of approximately 47 m. This is achieved, thanks to the amplifier chain discussed in detail in Section III-D. After the gain is not enough to saturate the tag anymore, it is still detectable up to

TABLE I
STATE-OF-THE-ART TAG-BASED RADAR SENSORS WITH HIGH RELEVANCE TO THIS WORK

Ref.	Year	Waveform	Freq. (GHz)	BW* (GHz)	P_{TX} (dBm)	$G_{\mathrm{TX,f}}$ (dBi)	$G_{\mathrm{RX,h}}$ (dBi)	$G_{\mathrm{TX,h}}$ (dBi)	$G_{\mathrm{RX,f}}$ (dBi)	Range (m)	$P_{\mathrm{DC,tag}}$ (mW)
This	2022	FMCW	79 / 79&158	4 / 10	9	28	34	12	12	80	89.1
[21]	2020	FMCW	61 / 122	8	6	21	22.2	7.5	7.1	23	132
[35]	2020	FMCW	2.9 / 5.8	0.16	34.7	13	14	#	#	40	0
[35]	2020	FMCW	9.3 / 18.6	0.16	40	15	15	#	#	15	0
[17]	2008	FMCW	5.95 / /11.9	0.2	20	22	22	5.5	2.8	58	0
[36]	2016	PRN	9.4 / 18.8	0.025	32.4	38	43	0.2	0.2	180	0
[37]	2013	FMCW†	77 / 77	2.5	15	40	40	16	16	22	0

*Refers to the harmonic bandwidth. This system is designed to utilize up to 10 GHz, while 4 GHz were used in the measurements.
#No gain is given in the publication.
† Based on the sweep of the intermodulation signal of two frequencies.

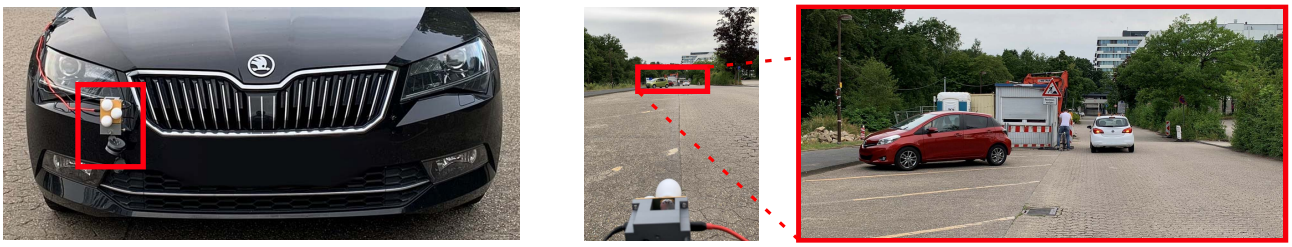

Fig. 17. Measurement scenario to showcase the harmonic approach. The harmonic radar system is mounted to a car's towing eye. Down the street, the bicycle is located near a construction site hut and cars.

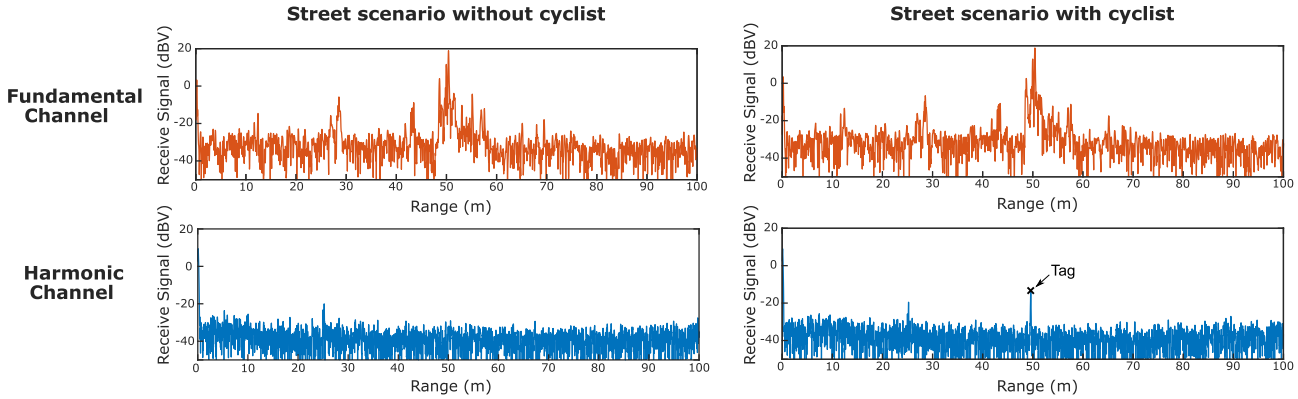

Fig. 18. Comparison of both the RX channels for the scenario depicted in Fig. 17 with and without the cyclist. Because of the strong reflections of the car and construction hut, the cyclist is completely invisible in the conventional radar measurement. The tag, however, is clearly visible in a nearly clutter-free harmonic RX channel.

a distance of approximately 80 m. This compares very well to other state-of-the-art tag-based radar systems presented in Table I. This is in part thanks to using an active tag. Thereby the power received at the system can be calculated as

$$P_{\mathrm{RX}} = P_{\mathrm{sat}} + G_{\mathrm{TX},h} + G_{\mathrm{RX},h} - \mathrm{FSPL}_h \tag{16}$$

as long as the power received at the tag meets the condition

$$P_{\mathrm{RX,tag}} = P_{\mathrm{TX}} + G_{\mathrm{TX},f} + G_{\mathrm{RX},f} - \mathrm{FSPL}_f > -57\ \mathrm{dBm} \tag{17}$$

to achieve saturation. This reduction of the target detection to a one-way propagation helps overcome the high free-space path loss at frequencies of up to 162 GHz.

To showcase the bicycle detection capabilities of the presented system in demanding measurement scenarios, an outdoor experiment was conducted. Therefore, the harmonic radar system was mounted to a car at its towing eye. A pedal cyclist was subsequently placed approximately 50 m down the street between a construction hut and a car. To detect the pedal cyclist in this scenario, which is shown in Fig. 17, is very demanding for the reasons discussed in Section I. To illustrate this problem, Fig. 18 shows a comparison of both the RX channels for the same scenario with and without the cyclist, including the harmonic tag.

In this comparison, the pedal cyclist does not generate additional, distinguishable targets in the conventional radar measurement at the fundamental frequency. Differences in the

two measurements are minimal, with one peak at 56 m actually being stronger without the cyclist covering a target with a larger RCS. In the harmonic channel, the tag located at the cyclist is the strongest target. Therefore, the tag allows for the detection of the pedal cyclist despite the difficult conditions. As the measurements were conducted for the presented, static environment, micro-Doppler extraction could not be carried out as a direct comparison. However, the large range to the bicycle of 50 m combined with the strong clutter surrounding it is expected to make a micro-Doppler-based detection very difficult, especially with the necessary robustness to ensure reliability. In the future, the presented system can be used for further investigations with dynamic scenarios. Apart from the tag's signal, the harmonic channel is nearly clutter-free with just one additional peak at just over 25 m. This peak is present in both the measurements and is a parasitic measurement of the construction site hut at half the distance. This effect has since been investigated in [38], and therefore should be caused by a coupling of the fundamental TX ramp into the RX. In future MIMO systems, it can likely be solved using the fundamental transceiver presented in Section III as separate TX chips.

VI. Conclusion

In this article, we presented a system capable of conducting conventional radar measurements and detecting harmonic RFID tags simultaneously. This allows for regular automotive radar measurements to increase traffic safety, while detecting cyclists with their lower RCS in a separate, nearly clutter-free RX channel.

We presented the necessary chipset, consisting of a fundamental and harmonic transceiver, respectively, as well as the VCO and harmonic RFID tag. The design considerations of the amplifier chain of the tag were presented in detail. Therefore, we introduced the gain per current metric and increased it using small transistors with a current density below peak f_{T}. In addition, we presented the PCBs of the harmonic radar system and the tag, including waveguide transitions covering the full W- and D-bands, respectively.

Finally, system measurements for a complicated traffic scenario were carried out. Therein, the presence of a cyclist was not detectable in a conventional radar measurement, while the tag was safely detected in a nearly clutter-free RX channel. The realized range of 80 m compares well to the state-of-the-art and is sufficient for city traffic, where bicycle accidents happen almost exclusively.

Acknowledgment

The authors would like to thank Infineon Technologies AG, Neubiberg, Germany, for the fabrication of the chips. They would also like to thank Bent Walther and Jonas Wagner for their valuable help throughout the realization of this work.

References

[1] J. Ziegler et al., "Making Bertha drive—An autonomous journey on a historic route," *IEEE Intell. Transp. Syst. Mag.*, vol. 6, no. 2, pp. 8–20, Apr. 2014.

[2] U. Franke et al., "Making Bertha see," in *Proc. IEEE Int. Conf. Comput. Vis. Workshops*, Dec. 2013, pp. 214–221.

[3] J. Dickmann et al., "Making Bertha see even more: Radar contribution," *IEEE Access*, vol. 3, pp. 1233–1247, 2015.

[4] I. Bilik, O. Longman, S. Villeval, and J. Tabrikian, "The rise of radar for autonomous vehicles: Signal processing solutions and future research directions," *IEEE Signal Process. Mag.*, vol. 36, no. 5, pp. 20–31, Sep. 2019.

[5] S. Sun, A. P. Petropulu, and H. V. Poor, "MIMO radar for advanced driver-assistance systems and autonomous driving: Advantages and challenges," *IEEE Signal Process. Mag.*, vol. 37, no. 4, pp. 98–117, Jul. 2020.

[6] M. Schroter et al., "The EU DOTSEVEN project: Overview and results," in *Proc. IEEE Compound Semiconductor Integr. Circuit Symp. (CSICS)*, Oct. 2016, pp. 1–4.

[7] J. Lee, Y.-A. Li, M.-H. Hung, and S.-J. Huang, "A fully-integrated 77-GHz FMCW radar transceiver in 65-nm CMOS technology," *IEEE J. Solid-State Circuits*, vol. 45, no. 12, pp. 2746–2756, Dec. 2010.

[8] C. Waldschmidt, J. Hasch, and W. Menzel, "Automotive radar—From first efforts to future systems," *IEEE J. Microw.*, vol. 1, no. 1, pp. 135–148, Jan. 2021.

[9] S. B. J. Gowdu, A. Schwind, R. Stephan, and M. A. Hein, "Monostatic RCS measurements of representative road traffic objects in the 76 …81 GHz frequency band," in *Proc. IEEE Radar Conf.*, Sep. 2020, pp. 1–6.

[10] W.-J. Liao, Y.-C. Hou, C.-C. Tsai, T.-H. Hsieh, and H.-J. Hsieh, "Radar cross section enhancing structures for automotive radars," *IEEE Antennas Wireless Propag. Lett.*, vol. 17, no. 3, pp. 418–421, Mar. 2018.

[11] C. Charlo, S. Meric, and R. Gillard, "RCS-enhancement for improving the detectability of bikes in road safety applications," in *Proc. 17th Eur. Radar Conf. (EuRAD)*, Jan. 2021, pp. 222–225.

[12] P. Held, D. Steinhauser, A. Kamann, A. Koch, T. Brandmeier, and U. T. Schwarz, "Micro-Doppler extraction of bicycle pedaling movements using automotive radar," in *Proc. IEEE Intell. Vehicles Symp. (IV)*, Jun. 2019, pp. 744–749.

[13] D. Belgiovane and C.-C. Chen, "Micro-Doppler characteristics of pedestrians and bicycles for automotive radar sensors at 77 GHz," in *Proc. 11th Eur. Conf. Antennas Propag. (EUCAP)*, Mar. 2017, pp. 2912–2916.

[14] E. Schubert, F. Meinl, M. Kunert, and W. Menzel, "High resolution automotive radar measurements of vulnerable road users—Pedestrians & cyclists," in *IEEE MTT-S Int. Microw. Symp. Dig.*, Apr. 2015, pp. 1–4.

[15] D. Steinhauser, P. Held, B. Thoresz, and T. Brandmeier, "Towards safe autonomous driving: Challenges of pedestrian detection in rain with automotive radar," in *Proc. 17th Eur. Radar Conf. (EuRAD)*, Jan. 2021, pp. 409–412.

[16] A. Singh and V. M. Lubecke, "Respiratory monitoring and clutter rejection using a CW Doppler radar with passive RF tags," *IEEE Sensors J.*, vol. 12, no. 3, pp. 558–565, Mar. 2012.

[17] D. Psychoudakis, W. Moulder, C.-C. Chen, H. Zhu, and J. L. Volakis, "A portable low-power harmonic radar system and conformal tag for insect tracking," *IEEE Antennas Wireless Propag. Lett.*, vol. 7, pp. 444–447, 2008.

[18] B. G. Colpitts and G. Boiteau, "Harmonic radar transceiver design: Miniature tags for insect tracking," *IEEE Trans. Antennas Propag.*, vol. 52, no. 11, pp. 2825–2832, Nov. 2004.

[19] T. T. Braun, J. Schopfel, C. Schweer, and N. Pohl, "A harmonic automotive radar for bicycle detection with RFID tags at 79/158 GHz," in *IEEE MTT-S Int. Microw. Symp. Dig.*, Jun. 2022, pp. 526–529.

[20] L. Piotrowsky and N. Pohl, "Spatially resolved fast-time vibrometry using ultrawideband FMCW radar systems," *IEEE Trans. Microw. Theory Techn.*, vol. 69, no. 1, pp. 1082–1095, Jan. 2021.

[21] S. Hansen, C. Bredendiek, G. Briese, and N. Pohl, "A compact harmonic radar system with active tags at 61/122 GHz ISM band in SiGe BiCMOS for precise localization," *IEEE Trans. Microw. Theory Techn.*, vol. 69, no. 1, pp. 906–915, Jan. 2021.

[22] J. Schoepfel, S. Kueppers, K. Aufinger, and N. Pohl, "A SiGe transceiver chipset for automotive radar applications using wideband modulation sequences," *Int. J. Microw. Wireless Technol.*, vol. 11, no. 7, pp. 676–685, May 2019.

[23] J. Schoepfel, T. T. Braun, S. Kueppers, K. Aufinger, and N. Pohl, "A fully differential hybrid coupler for automotive radar applications," in *Proc. 17th Eur. Microw. Integr. Circuits Conf. (EuMIC)*, Sep. 2022, pp. 107–110.

[24] C. Wang and G. Rebeiz, "A 2-channel 136–156 GHz dual down-conversion I/Q receiver with 30 dB gain and 9.5 dB NF using CMOS 22 nm FDSOI," in *Proc. IEEE Radio Freq. Integr. Circuits Symp. (RFIC)*, Jun. 2021, pp. 219–222.

[25] S. Voinigescu, *High-Frequency Integrated Circuits*. Cambridge, U.K.: Cambridge Univ. Press, 2013.
[26] M. H. White and M. O. Thurston, "Characterization of microwave transistors," *Solid-State Electron.*, vol. 13, no. 5, pp. 523–542, May 1970.
[27] B. Ardouin et al., "Transit time parameter extraction for the HICUM bipolar compact model," in *Proc. BIPOLAR/BiCMOS Circuits Technol. Meeting*, Oct. 2001, pp. 106–109.
[28] S. Fregonese et al., "A computationally efficient physics-based compact bipolar transistor model for circuit design—Part II: Parameter extraction and experimental results," *IEEE Trans. Electron Devices*, vol. 53, no. 2, pp. 287–295, Jan. 2006.
[29] S. Hansen, C. Bredendiek, G. Briese, and N. Pohl, "D-band FMCW radar sensor for industrial wideband applications with fully-differential MMIC-to-RWG interface in SIW," in *IEEE MTT-S Int. Microw. Symp. Dig.*, Jun. 2021, pp. 815–818.
[30] D. M. Pozar, *Microwave Engineering*. Hoboken, NJ, USA: Wiley, 2011.
[31] F. E. Goodwin and G. E. Moss, "Broad-band impedance matching into dielectric-filled waveguides," *IEEE Trans. Microw. Theory Techn.*, vol. MTT-11, no. 1, pp. 36–39, Jan. 1963.
[32] M. Sarkar and A. Majumder, "A novel broadband microstrip to waveguide transition at W band with high manufacturing tolerance suitable for MMIC packaging," in *IEEE MTT-S Int. Microw. Symp. Dig.*, Nov. 2018, pp. 1–4.
[33] N. Pohl and M. Gerding, "A dielectric lens-based antenna concept for high-precision industrial radar measurements at 24 GHz," in *Proc. Eur. Microw. Conf. (EuMC)*, Oct. 2012, pp. 731–734.
[34] L. Piotrowsky, J. Siska, C. Schweer, and N. Pohl, "Using FMCW radar for spatially resolved intra-chirp vibrometry in the audio range," in *IEEE MTT-S Int. Microw. Symp. Dig.*, Aug. 2020, pp. 791–794.
[35] G. Storz and A. Lavrenko, "Compact low-cost FMCW harmonic radar for short range insect tracking," in *Proc. IEEE Int. Radar Conf. (RADAR)*, Apr. 2020, pp. 642–647.
[36] Y.-T. Liu, M.-L. Hsu, H. Wang, and Z.-M. Tsai, "A differential miniature transponder for 9.4/18.8 GHz harmonic bee searching radar with low gain degradation from bee's body," in *IEEE MTT-S Int. Microw. Symp. Dig.*, May 2016, pp. 1–4.
[37] V. Viikari et al., "Technical solutions for automotive intermodulation radar for detecting vulnerable road users," in *Proc. VTC Spring-IEEE 69th Veh. Technol. Conf.*, Apr. 2009, pp. 1–5.
[38] S. Hansen and N. Pohl, "Experimental evaluation of filtering and isolation in highly integrated mmWave harmonic radar," in *Proc. 51st Eur. Microw. Conf. (EuMC)*, Apr. 2022, pp. 717–720.

Tobias T. Braun (Graduate Student Member, IEEE) was born in Düsseldorf, Germany, in 1996. He received the B.Sc. and M.Sc. degrees in electrical engineering and information technology from Technical University (TU) Dortmund, Dortmund, Germany, in 2016 and 2019, respectively. He is currently pursuing the Ph.D. degree at the Institute of Integrated Systems, Ruhr University Bochum, Bochum, Germany.

Since 2019, he has been a Research Assistant with the Institute of Integrated Systems, Ruhr University Bochum. His current research interests include integrated circuit and system design for automotive applications.

Mr. Braun was a recipient of the European Microwave Integrated Circuit Conference (EuMIC) Young Engineer Prize from European Microwave Week in 2021.

Jan Schöpfel (Graduate Student Member, IEEE) received the B.Sc. and M.Sc. degrees in electrical engineering and information technology from Ruhr University Bochum, Bochum, Germany, in 2014 and 2016, respectively.

Since 2017, he has been with the Institute for Integrated Systems, Ruhr University Bochum. His current research interests include concepts and integrated circuits for radar sensors for fully autonomous driving.

Mr. Schöpfel was a co-recipient of the EuMIC 2021 Best Student Paper Award.

Patrick Kwiatkowski (Graduate Student Member, IEEE) received the B.Sc. and M.Sc. degrees in electrical engineering and information technology from Ruhr University Bochum, Bochum, Germany, in 2015 and 2020, respectively. He is currently pursuing the Ph.D. degree at the Institute of Integrated Systems, Ruhr University Bochum.

His current research activities are in the field of novel multiple-input–multiple-output (MIMO) frequency-modulated continuous wave (FMCW) radar front-end concepts with a focus on antenna design.

Christian Schweer received the B.Eng. degree in electrical engineering and information technology from Hochschule Bochum, Bochum, Germany, in 2017, and the M.Sc. degree in electrical engineering and information technology from Ruhr University Bochum, Bochum, in 2021.

From 2018 to 2021, he has worked as a Student at the Institute for Integrated Systems, Ruhr University Bochum. Since finishing his M.Sc. degree, he has been with Kostal Automobil Elektrik GmbH & Company KG, Dortmund, Germany.

Klaus Aufinger (Member, IEEE) received the Diploma and Ph.D. degrees in physics from the University of Innsbruck, Innsbruck, Austria, in 1990 and 2001, respectively.

From 1990 to 1991, he was a Teaching Assistant with the Institute of Theoretical Physics, University of Innsbruck. In 1991, he joined Corporate Research and Development, Siemens AG, Munich, Germany, where he was involved in the investigation of noise in submicrometer bipolar transistors. He is currently with Infineon Technologies AG, Neubiberg, Germany, where he is also involved with device physics, technology development, and modeling of advanced SiGe technologies for high-speed digital and analog circuits.

Nils Pohl (Senior Member, IEEE) received the Dipl.Ing. and Dr.Ing. degrees in electrical engineering from Ruhr University Bochum, Bochum, Germany, in 2005 and 2010, respectively.

From 2006 to 2011, he was a Research Assistant with Ruhr University Bochum, where he has been an Assistant Professor since 2011. In 2013, he became the Head of the Department of mm-wave radar and high-frequency sensors with the Fraunhofer FHR, Wachtberg, Germany. In 2016, he became a Full Professor of integrated systems with Ruhr University Bochum. He has authored or coauthored more than 200 scientific articles and has issued several patents. His current research interests include ultrawideband mm-wave radar, design, and optimization of mm-wave integrated SiGe circuits and system concepts with frequencies up to 300 GHz and above, and frequency synthesis and antennas.

Dr. Pohl is a member of the Verband der Elektrotechnik, Elektronik und Informationstechnik (VDE), the Informationstechnische Gesellschaft (ITG), the European Microwave Association (EUMA), and the Union Radio-Scientifique Internationale (URSI). He was a recipient of the Karl-Arnold Award in 2013 and the IEEE MTT Outstanding Young Engineer Award in 2018. He was a co-recipient of the 2009 EEEfCom Innovation Award, the Best Paper Award at EuMIC 2012, the Best Demo Award at IEEE Radio and Wireless Week (RWW) 2015, and the Best Student Paper Awards at RadarConf 2020, RWW 2021, and EuMIC 2021.